

Post-treatment of Plasma-Sprayed Amorphous Ceramic Coatings by Spark Plasma Sintering

T. Chraska, Z. Pala, R. Mušálek, J. Medřický, and M. Vilémová

(Submitted June 6, 2014; in revised form October 20, 2014)

Alumina-zirconia ceramic material has been plasma sprayed using a water-stabilized plasma torch to produce free standing coatings. The as-sprayed coatings have very low porosity and are mostly amorphous. The amorphous material crystallizes at temperatures above 900 °C. A spark plasma sintering apparatus has been used to heat the as-sprayed samples to temperatures above 900 °C to induce crystallization, while at the same time, a uniaxial pressure of 80 MPa has been applied to their surface. After such post-treatment, the ceramic samples are crystalline and have very low open porosity. The post-treated material exhibits high hardness and significantly increased flexural strength. The post-treated samples have a microstructure that is best described as nanocomposite with the very small crystallites embedded in an amorphous matrix.

Keywords ceramics, heat treatment, nanostructured materials

1. Introduction

Thermally, sprayed ceramic coatings are one of the most wear-resistant coatings widely used in many large-scale industrial applications. The quest for thick nanostructured ceramic coatings, which could demonstrate improved properties as compared to their conventional counterparts, has led to development of two major approaches in thermal spraying. One approach takes advantage of available nanocrystalline powders that are deposited onto a substrate by a thermal spray method while retaining its nanocrystallinity. It either utilizes nanoparticles suitably agglomerated into micron-sized feedstock powder (Ref 1) or the nanoparticles of the original powder are suspended in a suitable liquid and deposited via thermal spraying of liquid suspension feedstock (e.g., Ref 2). Thermal spraying parameters in the first case are set to ensure that a certain fraction of the agglomerated powder will not be melted during the deposition process. The resulting microstructure thus contains both the unmelted nanocrystalline agglomerates and conventional splats formed from melted droplets. In the

case of liquid suspension, the resulting microstructure of deposits is very fine and contains a mixture of thin splats, unmolten irregular particles, and solidified spherical particles.

The second approach makes use of suitable liquid precursors that are fed into a plasma jet to form nanoparticles by physical and chemical processes in flight (precipitation of solute). The liquid precursors are mainly inorganic salts and metallo-organic compounds dissolved in water or in organic solvents (Ref 2). The processes occurring during solution thermal spraying and the resulting microstructures are more complicated than in suspension spraying.

A completely different approach to achieving nanostructured coating by thermal spraying for certain ceramic materials is presented in this paper. It has been previously reported that ceramic materials with near-eutectic composition can solidify as fully or partially amorphous solids due to rapid solidification (e.g., Ref 3). For example, plasma-sprayed deposits of ternary eutectic $\text{Al}_2\text{O}_3\text{-ZrO}_2\text{-SiO}_2$ materials will be almost completely amorphous in the as-sprayed state (Ref 4). It has been also shown that appropriate heat treatment of these amorphous deposits (Ref 5) leads to solid state crystallization and introduces nanocrystallites in the deposits.

This paper reports on nanocomposite ceramic material prepared by post-treatment of amorphous plasma-sprayed ceramic coatings of the above-mentioned ternary eutectic. The post-treatment encompassed the influence of increased temperature and applied external pressure and was done by Spark plasma sintering (SPS), also referred to as Field assisted sintering (FAST) or Pulsed Electric Current Sintering (PECS) (Ref 6). There are two main reasons for using SPS for the post-treatment. First of all, the heat is generated by pulsed DC current passing directly through a small graphite die that contains the ce-

This article is an invited paper selected from presentations at the 2014 International Thermal Spray Conference, held at May 21–23, 2014, in Barcelona, Spain and has been expanded from the original presentation.

T. Chraska, Z. Pala, R. Mušálek, J. Medřický, and M. Vilémová, Institute of Plasma Physics ASCR, Prague, Czech Republic. Contact e-mail: tchraska@ipp.cas.cz.

ramic sample. The small volume of the heated parts in SPS enables to achieve considerably higher heating and cooling rates than those achievable in conventional ovens or hot presses (Ref 7). Heating the as-sprayed amorphous samples above a certain temperature will cause crystallization in solid state. Secondly, compressing the as-sprayed deposits at raised temperature should lead to reduction of their inherent porosity and prevent porosity increase related to crystallization shrinkage.

The use of SPS for post-processing of thermally sprayed deposits is not very common, as the SPS equipment has only recently become more widespread. Some of the first published results are those of Prawara et al. (Ref 8) and Khor et al. (Ref 9) that reported significantly enhanced density and reduced porosity of plasma-sprayed ceramic coatings. SPS was also used to change phase content in plasma-sprayed hydroxyapatite (Ref 10) or increase carbon content in decarburized plasma-sprayed WC-Co coatings (Ref 11). The use of SPS for sintering of powders processed by plasma spraying is a little more common (e.g., Ref 12 or 13).

2. Experimental

The powder feedstock material is based on the bulk cast ceramic material called Eucor™ (Ref 14) that was crushed to powder and sieved to particle size range of 63–100 μm . Its near-eutectic composition was determined by semi-quantitative x-ray fluorescence, and the powder feedstock contained 46.5 wt.% of Al_2O_3 , 34.5 wt.% of ZrO_2 , 14.5 wt.% of SiO_2 , and 4.5 wt.% of other oxides (of alkali and alkaline earth metals). The feedstock material was plasma sprayed in air at atmospheric pressure using the water-stabilized plasma torch WSP® 500 (IPP ASCR) operating at 160 kW power. The powder was

injected into the plasma jet by compressed air at a constant feed rate of 250 g/min and deposited onto mild steel substrates positioned 350 mm away from the torch nozzle. The substrate surfaces were treated for easy deposit removal to produce freestanding coating rectangles (25 × 100 mm). The final coatings thickness ranged from 1 to 1.8 mm. Disks of 19.8 mm in diameter were cut out of the freestanding coatings. Both top and bottom surfaces of the as-sprayed disks were ground and polished in order to have smooth coplanar surfaces.

Spark plasma sintering was carried out in SPS 10-4 device (Thermal Technology LLC) operating in rotary pump vacuum. In order to clearly evaluate degree of sintering in the material, two almost identical disks were put into the die on top of each other between the two punches. Total thickness of the two as-sprayed disks ranged from 2.6 to 3.5 mm. Graphite foil was used to prevent direct contact of the disks with the die and punches that are made of high-strength graphite. Initial sintering of the two disks was done at a maximum temperature of 1150 °C for a dwell time of 5 min and compressive pressure of 80 MPa. Process temperature was controlled by a thermocouple inserted into a hole in the bottom graphite punch. During sintering, changes of the punch position are recorded as it moves due to the material shrinkage and sintering (decrease of its volume), while the pressure is kept constant. Evolution of chosen process parameters during the initial SPS process is given in Fig. 1. Consecutively, a set of SPS post-treatment was carried out at temperatures of 950, 1000, 1050, 1100, 1145, 1200, and 1300 °C with only one as-sprayed disk in the die at any given temperature. Dwell time at each temperature was 10 min, and maximum compressive pressure was 80 MPa.

Microstructure, indents of hardness measurement, and fracture surfaces were characterized in low vacuum mode by scanning electron microscopy (SEM: EVO® MA 15, Carl Zeiss) and energy dispersive x-ray spectrometry

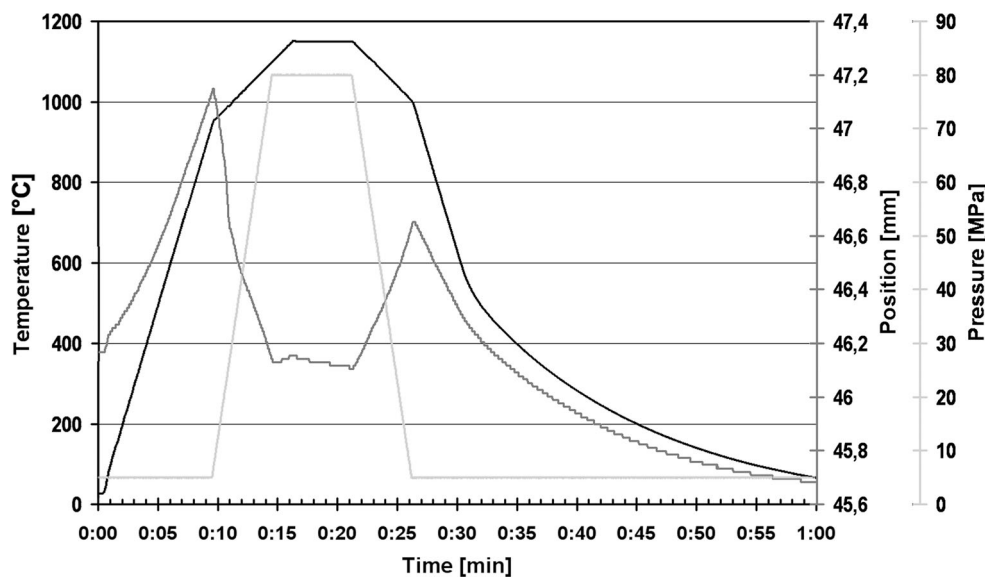


Fig. 1 Evolution of selected SPS process parameters during post-treatment

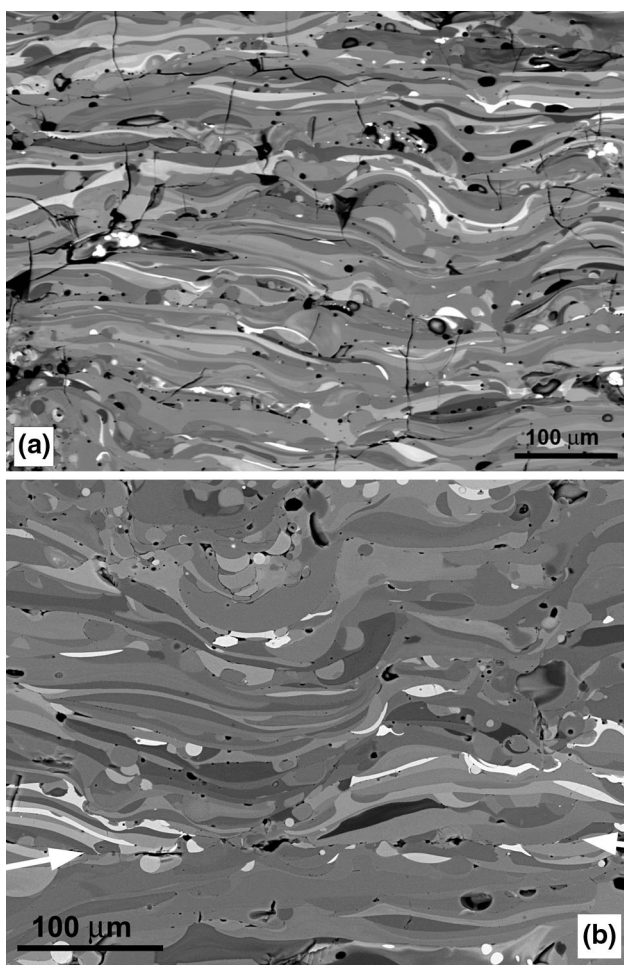


Fig. 2 SEM image (backscattered electrons) of un-etched polished cross section of as-sprayed sample (a) and SPS post-treated sample (b). Two white arrows indicate the location of interface between the two disks (b)

(EDS: XFlash 5010, Bruker). Powder diffractometer D8 Discover (Bruker) was used to complement microstructure not only with phase composition, but also with information about sizes of coherently scattering domains and estimation of degree of crystallinity. The diffractometer was used in standard Bragg-Brentano geometry with Cu $K\alpha$ radiation. Fixed primary slits were employed and beam knife placed above the sample surface, which lead to minimization of air scattering detected by 1D LynxEye detector. After the phase identification, the Rietveld refinement was carried out in TOPAS 4.2 software. Utmost care was devoted to proper routines of Rietveld analysis, especially in respect to correlation of refined parameters; in particular, the guidelines suggested in (Ref 15) were followed.

Vickers hardness was evaluated on polished cross sections by Nexus 4504 (Innovatest) hardness tester with 1 kg load so that the indents were bigger than typical splat size. Properties of individual splats were studied using instrumented indentation performed on Nano Indentation Tester (CSM Instruments Peseux) with Berkovich diamond indenter. All indentations (matrix of 20×19 indents) were carried out on the sample cross section with maximum load of 20 mN. The load-displacement data were evaluated according to the Oliver-Pharr theory (Ref 16).

Strength was evaluated by 3-point bending test of beams with typical dimensions $4 \times 3 \times 19$ mm using universal testing machine Instron 1362. Testing was carried out according to ASTM C1161-02, slightly modified with respect to the character of available samples. All surfaces and edges of the samples were ground by P220 and P500 SiC in order to remove any possible materials damage caused by the cutting process. Bearing cylinders were made of hardened steel (5 mm in diameter), and the support span was 14.55 mm. Loading with constant cross-head speed of 0.2 mm/min was applied until a macroscopic fracture of the specimen. From the known specimen

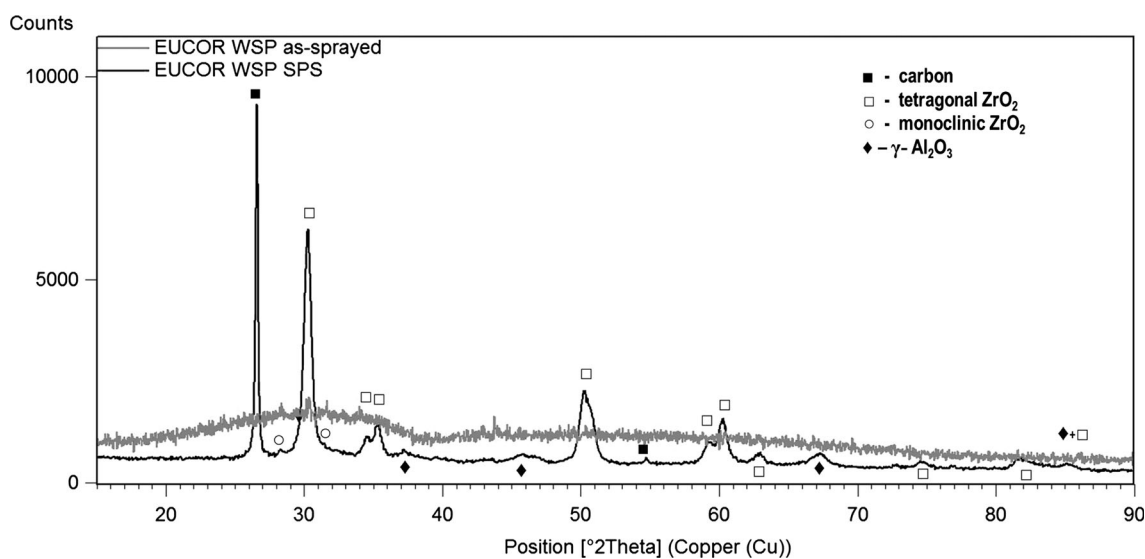


Fig. 3 XRD patterns of as-sprayed and SPS post-treated samples

dimensions, support span, and maximum load, 3-point bending (flexural) strength was evaluated according to ASTM C1161-02.

3. Results and Discussion

3.1 As-sprayed Material

Microstructure of the as-sprayed Eucor samples exhibits a pattern typical for plasma spraying (Fig. 2a). Most of the sample consists of thin splats (thin disk-shaped lamellae) with a few partially melted particles and cracks. Open porosity of the as-sprayed samples was around 3% as determined by Archimedeian (water immersion) technique. Individual splats in the coating have different chemical composition (different gray levels in Fig. 2) due to different proportions of Al and Zr oxides in the individual

powder particles. Most of the individual splats in the as-sprayed materials are, however, a blend of Al, Zr, and Si oxides that is chemically homogeneous within each splat. XRD analysis established the as-sprayed samples of Eucor materials to be almost completely amorphous (Fig. 3).

3.2 Post-treated Material

The sintering temperatures for SPS treatment were selected to be above the nano-crystallization temperature of approximately 950 °C (Ref 4). Microstructure of all the post-treated disks is similar to the one of the as-sprayed samples (Fig. 2b). However, there are only a few vertical cracks visible, and horizontal cracks between individual splats are no longer present. Open porosity of the post-treated samples was reduced down to 0.3%. The apparent closing of horizontal pores during sintering contributes to total sample shrinkage during SPS treatment. For exam-

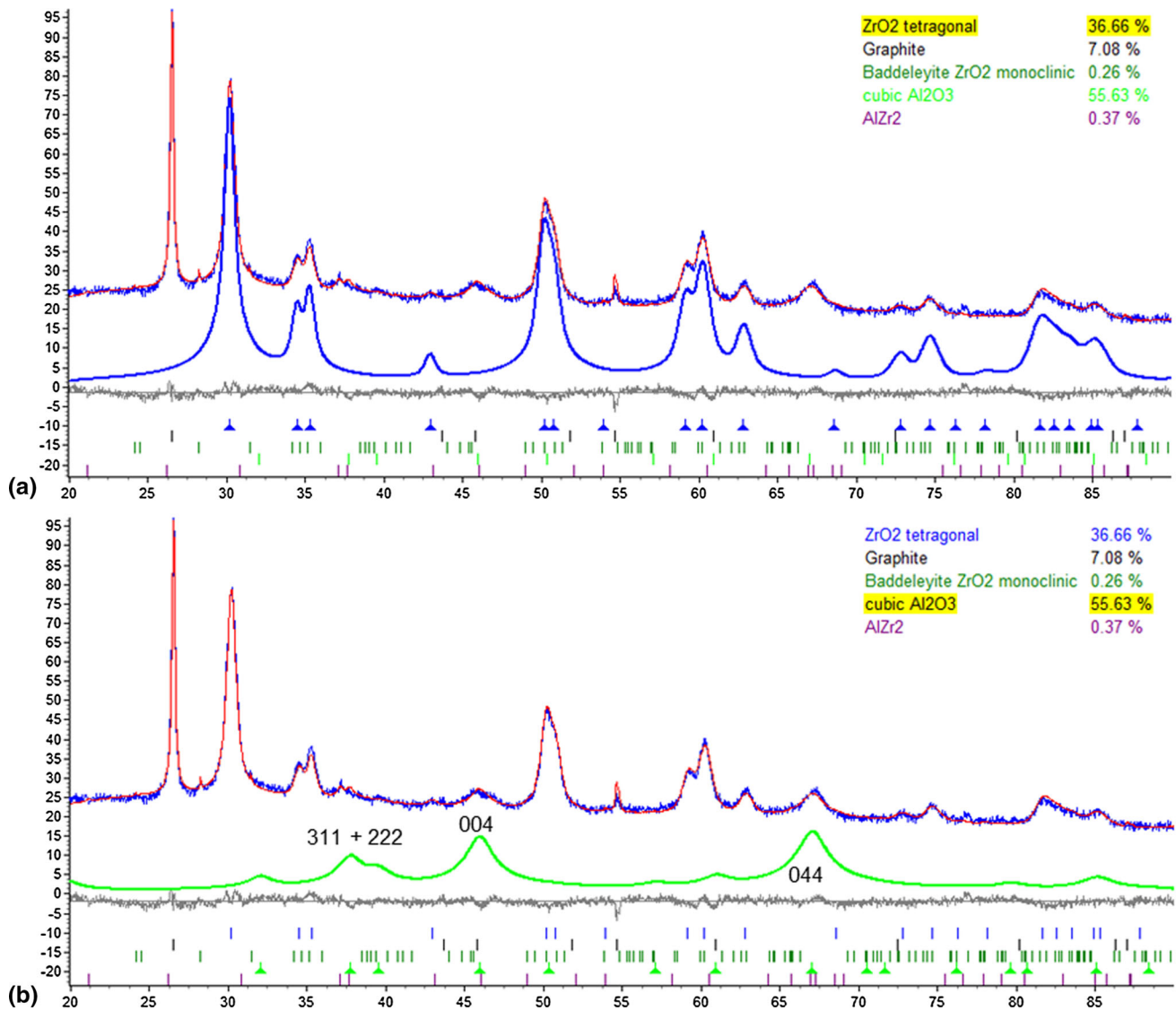


Fig. 4 Result of Rietveld analysis with partial diffraction patterns or more precisely structural models emanating from the refinement of tetragonal ZrO₂ (a) and cubic gamma alumina (b)

ple, the total shrinkage of the sample in Fig. 1 is $15 \pm 0.6\%$ as determined from the change of punch position in SPS. Shrinkage of 2% is due to crystallization as measured by thermomechanical analysis (Ref 4). The remaining 13% shrinkage is due to closing of cracks and pores during sintering. The other SPS-treated samples had the same total shrinkage with the exception of the one treated at 950 °C. The total shrinkage of the 950 °C sample was $13.1 \pm 0.6\%$.

XRD patterns of the post-treated material are presented in Fig. 3 and 4. Based on Rietveld refinement, there is only around 24 wt.% of remaining amorphous content in the material. The crystalline part contains 35 wt.% of tetragonal zirconia, 56 wt.% of gamma alumina, and very small amounts of monoclinic zirconia and quartz. The carbon is present only on as-received surfaces of SPS-treated samples and comes from the graphite foils. It is of no doubt that tetragonal ZrO_2 and the so-called gamma alumina are two dominant phases in the irradiated volume. However, the relative error of the obtained quantity of gamma alumina is higher when compared with standard errors of quantitative Rietveld refinement. This is not only due to the complexity of the gamma Al_2O_3 structure described as defect spinel $Al_{21+1/3}\square_{2+2/3}O_{32}$ (Ref 17), with \square denoting vacancy, but also due to nanometric grain sizes or more precisely coherently scattering domains in the case of XRD analyses. In our case, the partial diffraction pattern of nanosized gamma alumina has the character of consecutive broad diffraction profiles, as seen

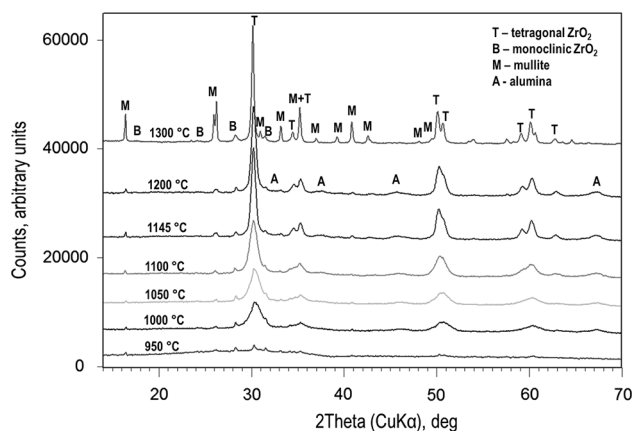


Fig. 5 Juxtaposition of seven diffraction patterns measured on samples with sintering temperature from 950 to 1300 °C

in Fig. 4(b), rather than narrower diffraction peaks embedded into flat background as in the case of tetragonal ZrO_2 (Fig. 4a). Hence, the interplay between the gamma alumina structural model and whole pattern background modeled by Chebychev 3rd polynome occurs, and this is reflected in the higher error. The average crystallite size of tetragonal ZrO_2 is 21 nm and that of gamma Al_2O_3 is 5.2 nm. As it was confirmed in previous work (Ref 4), the crystallites are also embedded in remains of amorphous matrix within each splat.

The juxtaposition of diffraction patterns measured on samples with sintering temperature from 950 to 1300 °C is in Fig. 5 and reveals not only changes in crystallinity, but also in diffraction profiles' shapes. The task of crystalline phase identification was, in this case, not a straightforward one with the main issue being mutual interplay between cubic and tetragonal aluminas especially in 1000 and 1050 °C sintered samples. We were unable to fully and reliably quantify presence of both γ and δ aluminas in these two samples only from XRD results and employment of Rietveld analysis. Nevertheless, in the sample subjected to SPS at 1300 °C, only a minor fraction of δ alumina amounting to less than 1 wt.% is present as most of it was transformed into mullite. Perhaps interestingly, the amount of monoclinic ZrO_2 increases from about 1 wt.% (1100 °C sample) to about 5 wt.% (1300 °C sample) with coherently scattering domain sizes diminishing

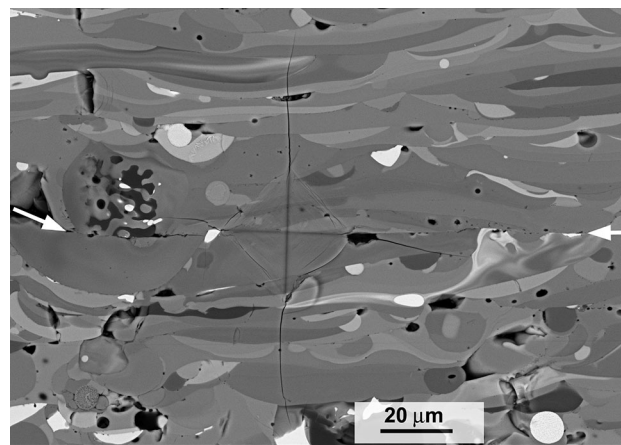


Fig. 6 SEM image (backscattered electrons) of un-etched polished cross section of the post-treated sample. Two white arrows indicate the location of interface between the two disks. Indentation from Vickers indenter is visible at the interface

Table 1 Summary of XRD measurement results

Sintering temperature	Crystallinity, %	Phase content, %				Crystallite size [nm]		
		Delta Al_2O_3	Tetragonal ZrO_2	ZrO_2 monoclinic	Mullite	Tetragonal	Monoclinic	Mullite
950	9.2		24.32	19.16	56.52	24	74	85
1100	82	50.92	42.33	1.27	5.48	10	72	74
1145	90	41.92	42.17	2.26	13.66	18	30	41
1200	92	43.11	41.41	2.01	13.47	17	36	31
1300	100	0.71	27.08	5.22	66.98	36	20	74

from about 70 to 20 nm. The evolution of crystallinity estimated by Rietveld refinement is also interesting, in particular rising from about 10 wt.% in 950 °C sample to 92 wt.% in 1200 °C sample and with 1300 °C sample reaching fully crystalline state. The XRD results are summarized in Table 1.

3.3 Mechanical Properties

To qualitatively evaluate bonding between the two sintered disks, Vickers hardness was measured at the interface between the two original disks and compared with values measured in the rest of the post-treated sample. Regardless of measurement location (including the interface between the original disks), Vickers hardness showed value of 1075 ± 60 HV1. Also the cracks emanating from the corners of the indent do not follow the original interface between the two disks (Fig. 6). These results confirm the assumption that the post-treatment sintering would create one monolithic material.

This result was further supported by comparison of flexural strength of as-sprayed and post-treated samples. Average flexural strength of the as-sprayed samples as determined from the 3-point bending tests was 53 ± 6 MPa. Average flexural strength of the initial double disk samples SPS treated at 1150 °C was 185 ± 12 MPa, which is more

than a threefold increase. The character of loading in both materials was also substantially different. For the as-sprayed sample, after reaching maximum force during bending, the force gradually decreased as failure gradually propagated through the material (Fig. 7a). On the other hand, the sintered material failed abruptly by a sudden release of the accumulated deformation energy at the maximum force. The original interface between the two disks did not play any significant role in the failure of the sintered material as can be seen from a fracture surface (Fig. 7b) and thus confirmed formation of well-sintered compact material.

Flexural strength measured on the set of single disk samples SPS treated at temperatures from 950 to 1200 °C was slightly lower than that of the initial double disk sample. However, the 1300 °C treated sample had flexural strength of 196 ± 15 MPa. This increase is related to the fact that this is the only sample that contains two-thirds of mullite nanocrystals, and the fracture surface is thus noticeably different (Fig. 8).

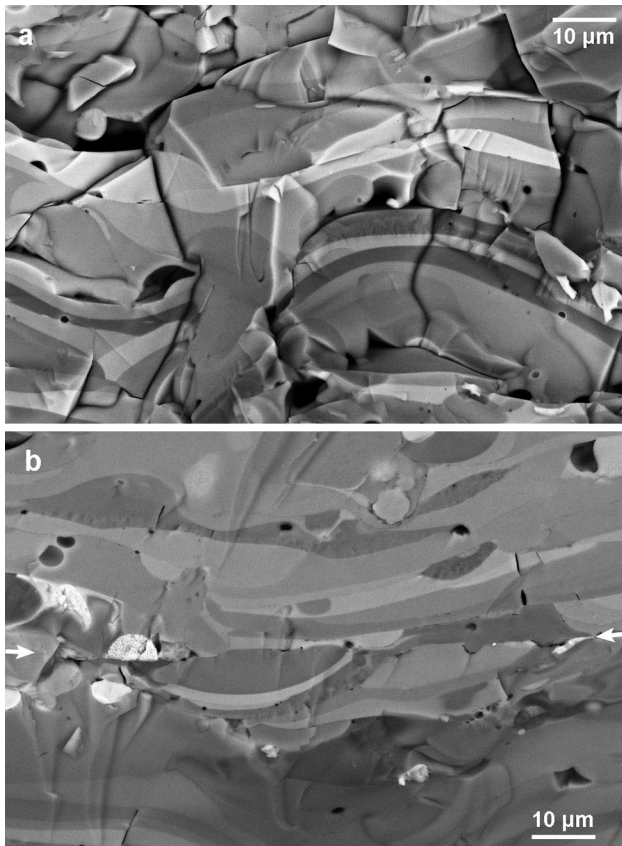


Fig. 7 SEM images (backscattered electrons) of fracture surface of as-sprayed sample (a) and sintered sample (b) near the interface of original disks (indicated by arrows)

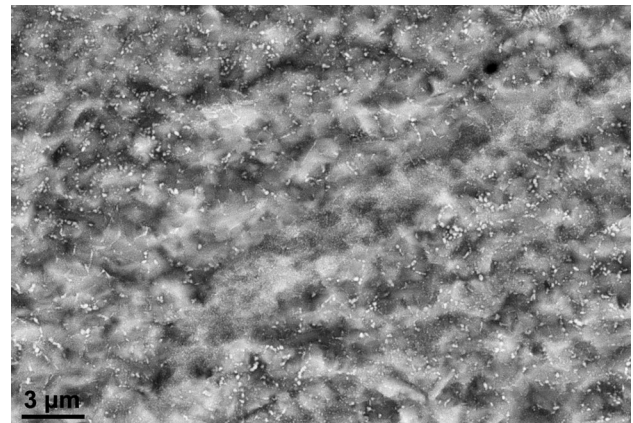


Fig. 8 SEM images (backscattered electrons) of fracture surface of sample sintered at 1300 °C

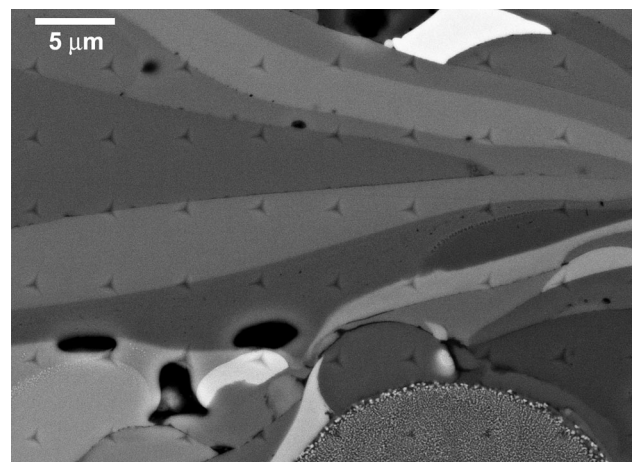
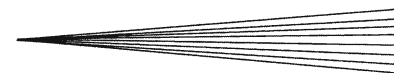


Fig. 9 SEM image (backscattered electrons) of un-etched polished cross section of the post-treated sample showing part of a nanoindentation matrix



Nanohardness measurements attempted to evaluate possible differences between individual splats of different chemical composition and thus phase content. The indentation matrix covered not only splats of various gray levels but also a coarse partially melted particle (Fig. 9). Most of the splats including the ZrO_2 -rich phase as well as Al_2O_3 -rich phase exhibit indentation hardness between 21 and 23 GPa and indentation modulus between 250 and 290 GPa. The hardness seems to be uninfluenced by the splat composition. However, in some cases, significant property variation was detected within certain individual splats experiencing scatter in hardness from 13 to 22 GPa. It is apparent from the back-scattered electron signal, the chemical composition is not homogenous within those splats.

4. Conclusions

Post-treatment of plasma-sprayed material by spark plasma sintering is a suitable technique for controlled crystallization and further compaction of as-sprayed deposits. The as-sprayed amorphous deposits were transformed into almost fully dense mostly crystalline material with negligible open porosity. The two major phases in sample sintered at 1150 °C, gamma alumina and tetragonal zirconia, are present in the form of nanocrystallites with average size 5.2 and 21 nm, respectively. The post-treated material is very well sintered since the interface between the two disks of the same material did not play any significant role in the failure. Similar sintering must have taken place in the rest of the as-sprayed material resulting in significantly improved cohesion between splats. Therefore, interfaces and cracks between splats in the post-treated sample do not present a viable path for failure propagation under mechanical loading unlike interfaces in as-sprayed deposits. The improved splat cohesion results in more than a threefold increase of flexural strength in the post-treated samples. Hardness values of 1075 HV1 in the post-treated sample are increased by about 30% when compared to values of 830 HV1 in the as-sprayed material. Samples sintered at 1300 °C are fully crystalline, contain about two-thirds of mullite phase in the form of nanocrystals, and exhibit the highest values of flexural strength of all post-treated samples.

Acknowledgment

Support by the Grant Agency of the Czech Republic under the Grant P107/12/1922 is acknowledged. Discussions and collaboration with P. Hausild as well as the

availability of the Nano Indentation Tester at the Faculty of Nuclear Science and Physical Engineering of Czech Technical University are gratefully appreciated.

References

1. R.S. Lima and B.R. Marple, Thermal Spray Coatings Engineered from Nanostructured Ceramic Agglomerated Powders for Structural, Thermal Barrier and Biomedical Applications: A Review, *J. Therm. Spray Technol.*, 2007, **16**(1), p 40-63
2. L. Pawlowski, Suspension and Solution Thermal Spray Coatings, *Surf. Coat. Technol.*, 2009, **203**(19), p 2807-2829
3. X. Zhou, V. Shukla, W.R. Cannon, and B.H. Kear, Metastable Phase Formation in Plasma-Sprayed ZrO_2 (Y_2O_3)- Al_2O_3 , *J. Am. Ceram. Soc.*, 2003, **86**(8), p 1415-1420
4. T. Chraska, K. Neufuss, J. Dubsky, P. Ctibor, and M. Klementova, Fabrication of Bulk Nanocrystalline Ceramic Materials, *J. Therm. Spray Technol.*, 2008, **17**(5-6), p 872-877
5. T. Chráska, J. Hostomský, M. Klementová, and J. Dubský, Crystallization Kinetics of Amorphous Alumina-Zirconia-Silica Ceramics, *J. Eur. Ceram. Soc.*, 2009, **29**(15), p 3159-3165
6. Z.A. Munir, D.V. Quach, and M. Ohyanagi, Electric Current Activation of Sintering: A Review of the Pulsed Electric Current Sintering Process, *J. Am. Ceram. Soc.*, 2011, **94**(1), p 1-19
7. S. Chanthapan, A. Rape, S. Gephart, A.K. Kulkarni, and J. Singh, Industrial Scale Field Assisted Sintering, *Adv. Mater. Processes*, 2011, **169**(7), p 21-26
8. B. Prawara, H. Yara, Y. Miyagi, and T. Fukushima, Park Plasma Sintering as a Post-spray Treatment for Thermally-Sprayed Coatings, *Surf. Coat. Technol.*, 2003, **162**(2-3), p 234-241
9. K.A. Khor, L.G. Yu, S.H. Chan, and X.J. Chen, Densification of Plasma Sprayed YSZ Electrolytes by Spark Plasma Sintering (SPS), *J. Eur. Ceram. Soc.*, 2003, **23**(11), p 1855-1863
10. L.G. Yu, K.A. Khor, H. Li, and P. Cheang, Effect of Spark Plasma Sintering on the Micro-structure and In Vitro Behavior of Plasma Sprayed HA Coatings, *Biomaterials*, 2003, **24**(16), p 2695-2705
11. H. Li, K.A. Khor, L.G. Yu, and P. Cheang, Microstructure Modifications and Phase Trans-formation in Plasma-Sprayed WC-Co Coatings Following Post-spray Spark Plasma Sintering, *Surf. Coat. Technol.*, 2005, **194**(1), p 96-102
12. J. Suffner, D. Wang, and H. Hahn, Enhancing Superplasticity of ZrO_2 (Y_2O_3)- Al_2O_3 Composites Prepared by Spark Plasma Sintering of Metastable Powders, *Mater. Sci. Eng. A*, 2010, **527**(29-30), p 7885-7892
13. X.R. Ren and W. Pan, Mechanical Properties of High-Temperature-Degraded Yttria-Stabilized Zirconia, *Acta Mater.*, 2014, **69**, p 397-406
14. Information about material supplier, <http://www.eutit.com/materialy.html>
15. L.B. McCusker, R.B. von Dreele, D.E. Cox, D. Loue, and P. Scardi, Rietveld Refinement Guidelines, *J. Appl. Crystallogr.*, 1999, **32**, p 36-50
16. X.W.C. Oliver and G.M. Pharr, An Improved Technique for Determining Hardness and Elastic Modulus Using Load and Displacement Sensing Indentation Experiments, *J. Mater. Res.*, 1992, **7**(6), p 1564-1583
17. L. Smrcek, V. Langer, and J. Krestan, γ -Alumina: Single Crystal X-Ray Diffraction Study, *Acta Cryst.*, 2006, **C62**, p i83-i84